

We are IntechOpen, the world's leading publisher of Open Access books Built by scientists, for scientists

6,900

Open access books available

185,000

International authors and editors

200M

Downloads

Our authors are among the

154

Countries delivered to

TOP 1%

most cited scientists

12.2%

Contributors from top 500 universities



WEB OF SCIENCE™

Selection of our books indexed in the Book Citation Index
in Web of Science™ Core Collection (BKCI)

Interested in publishing with us?
Contact book.department@intechopen.com

Numbers displayed above are based on latest data collected.
For more information visit www.intechopen.com



Application of Atomic Force Microscopy in Organic and Perovskite Photovoltaics

Chandra Shakher Pathak

Abstract

Atomic force microscopy (AFM) has become widely used technique in air, liquids, or vacuum to generate high-resolution topographic images of a surface having a nanometer-scale resolution. AFM gives the information about the morphology, phase composition etc. Photovoltaic materials have been attracting intense interest due to their performance and the morphology as well as quality of these materials affects their performance. AFM is now a day widely used technique for morphology and other electronic properties measurements at nanoscale for photovoltaic materials to understand their relation with device performance. This chapter describe the brief introduction of Kelvin probe force microscopy (KPFM) and conducting atomic force microscopy (CAFM) and their application in electrical characterization at nanoscale of organic and perovskite photovoltaic materials.

Keywords: AFM, KPFM, CAFM, Photoconductive AFM, Nano scale, Electrical properties, Surface potential

1. Introduction

Scanning tunneling microscopy (STM) was first introduced in 1982 and it is based on tunneling of electron between the metallic tip and sample surface and it is limited to the study of conducting surface [1]. After four years in 1986, the solution of this restriction was provided by atomic force microscopy (AFM) and it is based on the detection of attractive or repulsive forces [2]. AFM was used to analyze the surface morphology and used to measure the force of interaction between the AFM tip and the sample. AFM consists of a sharp tip having nanometer dimension which is attached to a cantilever is used to scan the sample surface. A laser beam focused on the cantilever which detects the bending of cantilever. The reflection of the laser beam is focused on photodiode detector. Deflection of the cantilever is monitored during the scanning and converted into surface image. AFM is generally operated in contact mode and tapping mode. AFM is the widely used tool for the characterization of materials surface at the nanoscale. AFM was developed to a very versatile technique by combination with other measurements methods. This chapter will cover the application of electrical mode of AFM specifically Kelvin probe force microscopy (KPFM) and conducting atomic force microscopy (CAFM).

1.1 Kelvin probe force microscopy

Lord Kelvin proposed macroscopic Kelvin probe method in 1898 to determine the contact potential difference (V_{CPD}) between a metallic plate and sample [Kelvin L., Contact electricity of metals *Phil. Mag.* 1898, 46, 82–120]. Later in 1991, KPFM was first introduced by Nonnenmacher *et al.* [3]. The KPFM mode is basically two-scan process. In the first scan topography of the surface is acquired in tapping mode along a single line profile. Following this, the mechanical excitation of the cantilever is turned off and in the second scan this topography is retraced at a certain lift height (LH) above the sample surface, recording local variations in contact potential difference (CPD). During the second scan, the tip-sample distance is constant and it is equal to $d_{AFM} + LH$, where d_{AFM} represent the tip-sample distance during the topographic scan. When the AFM tip is brought close to the sample surface, the electrostatic force is generated and it is proportional to the difference between their Fermi levels. If the work functions of the sample and the tip are different, electrons flow from the lower work function to the higher work function material to align their Fermi level and the system reach in charge equilibrium condition. The vacuum levels of the tip and sample are not the same and the surfaces of the sample and the tip are charged and an apparent V_{CPD} will form. Due to the V_{CPD} an electrical force acts on the contact area and this force can be nullified by applying a DC voltage and it is equal to the work function difference between tip and sample. The work function of the sample can be calculated when the tip work function is known from scanning a reference sample.

1.2 Conductive atomic force microscopy

Conductive atomic force microscopy (CAFM) is usually used to analyze the local variations in current of the sample. The AFM controller is used for applying dc bias through the substrate during measurements. The CAFM tip is connected through a low noise current amplifier to the AFM controllers to generate the current image. We can collect the current–voltage (I - V) characteristics by CAFM tip which can be contacted randomly at various positions of sample surface and I - V characteristics are collected at each position.

KPFM generates 3D mapping of surface electric potential and measure the local work function while CAFM generates the current map. CAFM is one of the simplest ways of characterizing electrical properties at high resolution is by applying voltage between the sample and a CAFM probe. Photoconductive AFM; current mapping under illumination is useful for correlating high resolution current mapping with the photovoltaic device performance. Now a day these two modes of AFM in electrical mode are widely used in all area of research; nanoelectronics field, solar cell, 2D materials and semiconductor industries, biology etc. This chapter consists the collection of some published work as well as some new results.

2. Organic photovoltaics

Conducting polymers have been attracting attention after their discovery by Shirakawa, MacDiarmid, and Heeger in 1977, who were awarded the Nobel Prize in Chemistry in 2000 for the discovery of conductive polymers [4, 5]. They used organic polymer polyacetylenes, which is a conjugate polymer and insulator and increased the conductivity of polyacetylene films by several orders of magnitude by chemical doping [4]. In recent years, there has been lot of research activity in the field of polymer electronics and attracted a lot of attention because of its high

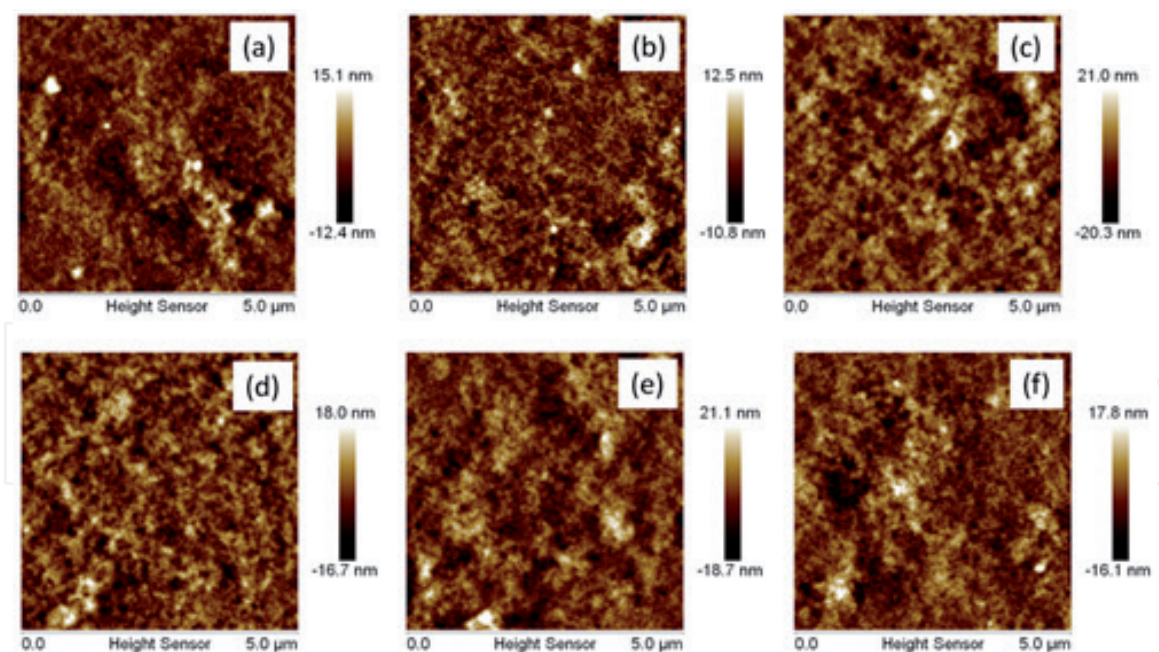


Figure 1.
 AFM images of PEDOT:PSS films modified with (a) 0% NMP 1% MeOH, (b) 0.1% NMP 1% MeOH, (c) 0.3% NMP 1% MeOH, (d) 0.5% NMP 1% MeOH, (e) 0.8% NMP 1% MeOH, and (f) 0% MeOH 0.5% NMP. Reproduced with permission from [16].

flexibility, light weight and solution process ability [6]. Applications of conducting polymers include organic light emitting diodes, organic thin film transistors, organic solar cells, actuators and sensors etc. [7–13]. AFM is usually used to measure the roughness, morphology and phase analyses of conductive polymer [13]. KPFM is used to measure the work function [14–20] and CAFM [18, 21, 22] used to measure the current of the organic solar cell materials. These two methods gives valuable insights in the structure and working mechanism of organic photovoltaic devices.

Poly(3,4-ethylenedioxythiophene)-poly (styrenesulfonate) (PEDOT:PSS) is a well-known conducting polymer because of its high conductivity, excellent thermal stability, transparency, structural stability and processability [23–25]. PEDOT:PSS polymer is a promising candidate as a transparent electrode for optoelectronic devices. PEDOT is made from ethylenedioxythiophene (EDOT) monomers. PEDOT is insoluble in many common solvents, and it is unstable in its neutral state. To improve its processability, water-soluble polystyrene sulfonate (PSS), can be added and the addition of PSS causes it to become soluble. During the polymerization, PSS acts as charge balancing dopant to yield PEDOT:PSS.

Figure 1 shows the height images and **Figure 2** shows the surface potential images of PEDOT:PSS films with co-solvents (N-Methyl-2-pyrrolidone (NMP) and methanol (MeOH)). The average root-mean-square roughness (RMS) values were found in the range 3.2–5.5 nm. Pristine PEDOT:PSS film was quite smooth with a RMS roughness of 2.6 nm. RMS roughness values of PEDOT:PSS films increases after co-solvents addition. Variation in the RMS roughness after addition of co-solvents indicates the morphological change that arises from the conformation of the polymer chain [16]. The estimated average work function of co-solvents doped PEDOT:PSS thin films range from 4.63 to 4.82 eV as compared to 4.9 eV for the pristine PEDOT:PSS film [16]. Work function can be calculated with the following Equation [16, 27].

$$V_{CPD} = \frac{\phi_{tip} - \phi_{sample}}{-e} \quad (1)$$

where V_{CPD} is the contact potential different measured by KPFM in volts, ϕ_{tip} and ϕ_{sample} are the work functions of tip and sample in eV, respectively, while e is the electronic charge.

Figure 3 shows the current map of bare and NMP doped PEDOT:PSS films. Bare PEDOT:PSS has less current as compared to NMP doped PEDOT:PSS film as shown in **Figure 3** [28]. This shows the reduction of more PSS from the surface for NMP doped PEDOT:PSS film. Hosseini *et al.* [22] also reported higher current for ethylene glycol (EG) doped PEDOT:PSS film.

Figure 4 shows topography, surface potential images and corresponding line profile of bare and NMP doped PEDOT:PSS films. Bare PEDOT:PSS has work function of 4.90 eV and 4.77 eV for NMP doped PEDOT:PSS film [16, 28]. Line profile shows the homogenous distribution of surface potential. We also showed that the work function was reduced with the addition of dimethyl sulfoxide (DMSO) solvent in PEDOT:PSS [15].

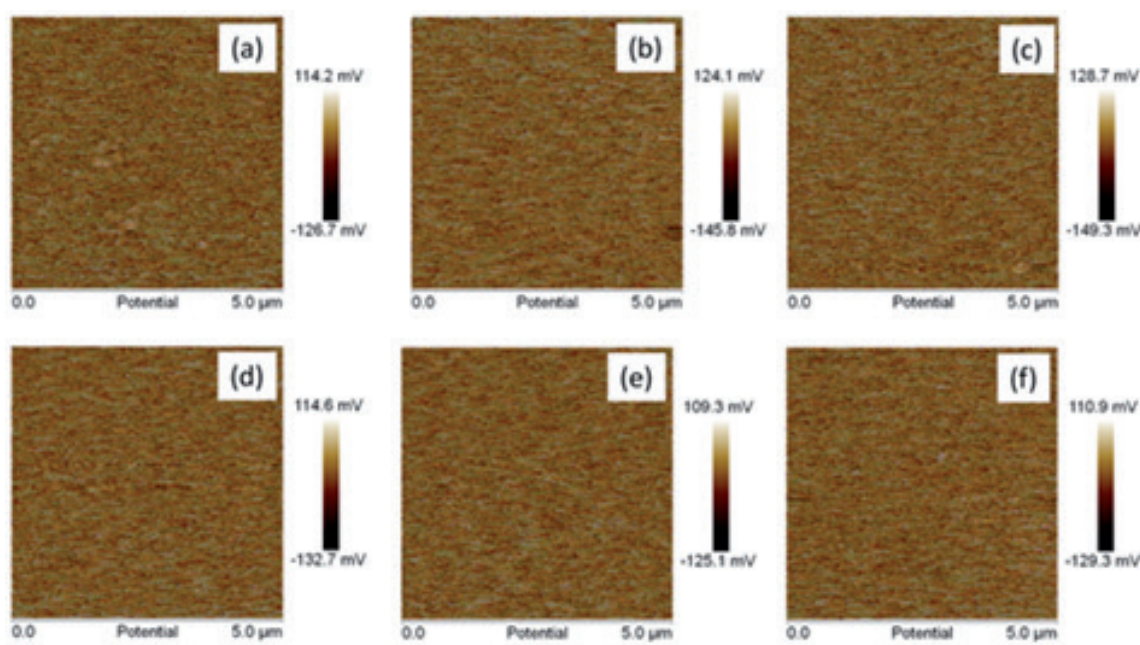


Figure 2. Potential images of PEDOT:PSS films modified with (a) 0% NMP 1% MeOH, (b) 0.1% NMP 1% MeOH, (c) 0.3% NMP 1% MeOH, (d) 0.5% NMP 1% MeOH, (e) 0.8% NMP 1% MeOH, and (f) 0% MeOH 0.5% NMP. Reproduced with permission from [26].

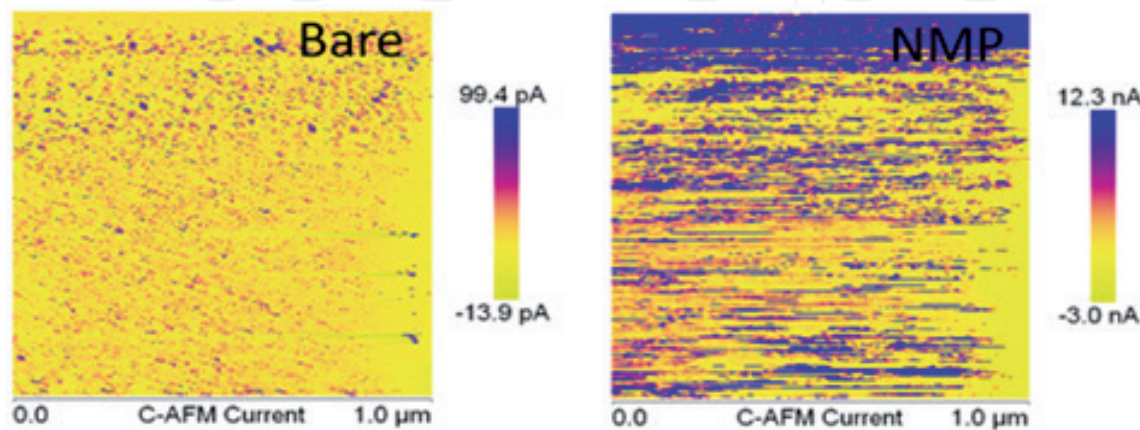


Figure 3. CAFM images of bare and NMP doped PEDOT:PSS films. Reproduced with permission from [28].

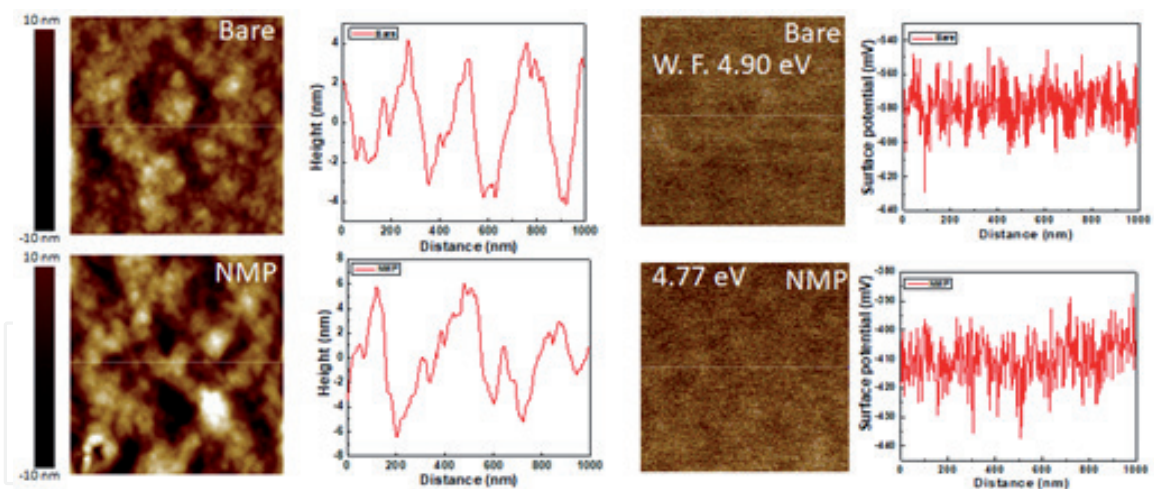


Figure 4.
 Topography, CPD images and corresponding line profile of bare and NMP doped PEDOT:PSS films.
 Reproduced with permission from [28].

3. Perovskite photovoltaic

The last 10 years has seen a new photovoltaic (PV) technology being discovered and developed at a rate greater than any previous energy harvesting technology with research fuelled by the facile, low cost large area solution processing routes available for device fabrication. These devices, known as organic–inorganic metal halide perovskites have certified power conversion efficiencies (PCEs) $> 25\%$ [29], comparable values to the incumbent technologies but available at a fraction of the materials and processing costs. The perovskite thin films are typically polycrystalline ones, comprising microstructures such as grains and grain boundaries (GBs). Recently some of research groups have performed the microscopic investigation and suggested that the grain boundaries (GBs) in planar perovskite solar cells have beneficial [30, 31]. Hence engineering of the perovskite films and the microscopic investigation is essential for the further improvement in the properties of perovskite photovoltaics. CAFM and KPFM have been widely used to characterize the local properties of perovskite thin films at nanoscale to see the changes in electrical properties specially to improve the performance and stability of perovskite photovoltaics. CAFM [30–37] and KPFM [32, 38–40] have been used to characterize the local properties of perovskite thin films. Such studies suggested that GBs have beneficial effects due to efficient photogenerated charge carrier separation and collection at GBs [30, 31]. Downward- as well as upward- band bending at GBs were reported from KPFM measurements, depending on the GB composition [41]. Zhao *et al.* [32] measured the photocurrent of FTO/compactTiO₂/mesoporousTiO₂ + CH₃NH₃PbI₃/CH₃NH₃PbI₃ film and found the photo current intensities were higher on the center of the grain than on the defect position, whereas the larger grain size leads to the higher photocurrent on the center. They also reported that the dark current intensities increased dramatically in the defect position, suggesting a high conductive character for defect position. Li *et al.* [31] fabricated CH₃NH₃PbI₃/mTiO₂/c-TiO₂/FTO typical device and performed c-AFM measurements under steady illumination of power 14 mW/cm² on CH₃NH₃PbI₃ surface from the top and showed that the photocurrent flows through the GBs are negligible at 0 V bias, while the major photocurrents form on the grains. However, with the low bias the photocurrents at the GBs become much higher than those of the grains. Xu *et al.* [35] also observed higher current near GBs for CH₃NH₃PbI₃-PCBM structure under high vacuum and dark conditions.

Kutes *et al.* [34] performed photoconductive AFM for methylammonium lead iodide ($\text{CH}_3\text{NH}_3\text{PbI}_3$)/c- TiO_2 /FTO/glass structure and the schematic diagram of the photoconductive (CAFM under illumination) AFMs configuration shown in **Figure 5**. They observed higher current in grains than grain boundary (GB) as shown in **Figure 6**.

Yun *et al.* [30] also used CAFM and KPFM technique to investigate the role of GBs and the schematics shown in **Figure 7**. They observed the higher CPD at grain boundary with illumination and current near GBs for $\text{CH}_3\text{NH}_3\text{PbI}_3/\text{TiO}_2/\text{FTO}/\text{glass}$ heterojunction structure than in the grains as shown in **Figures 8 and 9**.

They found that the higher current collection near GBs is consistent with KPFM results, which indicates that photogenerated carriers are more efficiently separated and transported along the GBs. Lower CPD at the GBs under the dark condition implies that downward band bending is present at GBs. KPFM is widely used for photovoltaics to analyses the work function of perovskite materials.

We prepared the MAPI films as described by Liu *et al.* [42] and they dipped PbI_2 film on $\text{CH}_3\text{NH}_3\text{I}$ solution. Here we spin casted $\text{CH}_3\text{NH}_3\text{I}$ in 1 ml isopropanol on mesoporous PbI_2 film and annealed the prepared films at 70° to 110°C for 10 minutes. **Figure 10** shows the height image and current–voltage characteristics of $\text{CH}_3\text{NH}_3\text{PbI}_3$ (MAPI) films on FTO annealed at 70° , 90° and 110°C for 10 min respectively. Which shows the higher grain size for 70°C annealed perovskite film (**Figure 10a**) and the current was in pA for all three samples.

After the temperature variation CAFM studies, We prepared mesoporous PbI_2 scaffolds MAPI films on FTO and annealed at 100°C were analyzed in details. CAFM and KPFM with and without illumination measurements were done and the schematics of these measurements are shown in **Figure 11** and results are shown in **Figures 12 and 13**. At dark and with the illumination of 532 nm laser having intensity of $0.6\text{ W}/\text{cm}^2$ shows homogeneous higher current near GBs. KPFM also shows

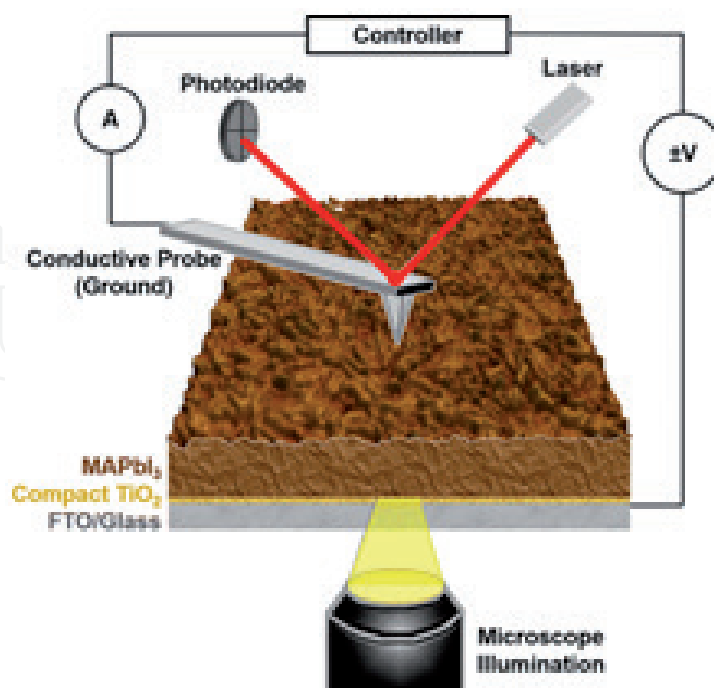


Figure 5. Schematic diagram of the photoconductive AFMs configuration where the perovskite solar cell (PSC) is illuminated from below through a transparent-conducting cathode (FTO/glass) while measuring local current with a positionable conductive AFM probe anode from above. This diagram includes a 3D rendered, $3\text{ }\mu\text{m} \times 3\text{ }\mu\text{m}$, topographic AFM image of a methylammonium lead triiodide (MAPbI_3) thin film, along with a schematic cross section of the PSC containing a compact TiO_2 electron transport layer reproduced with permission from [34].

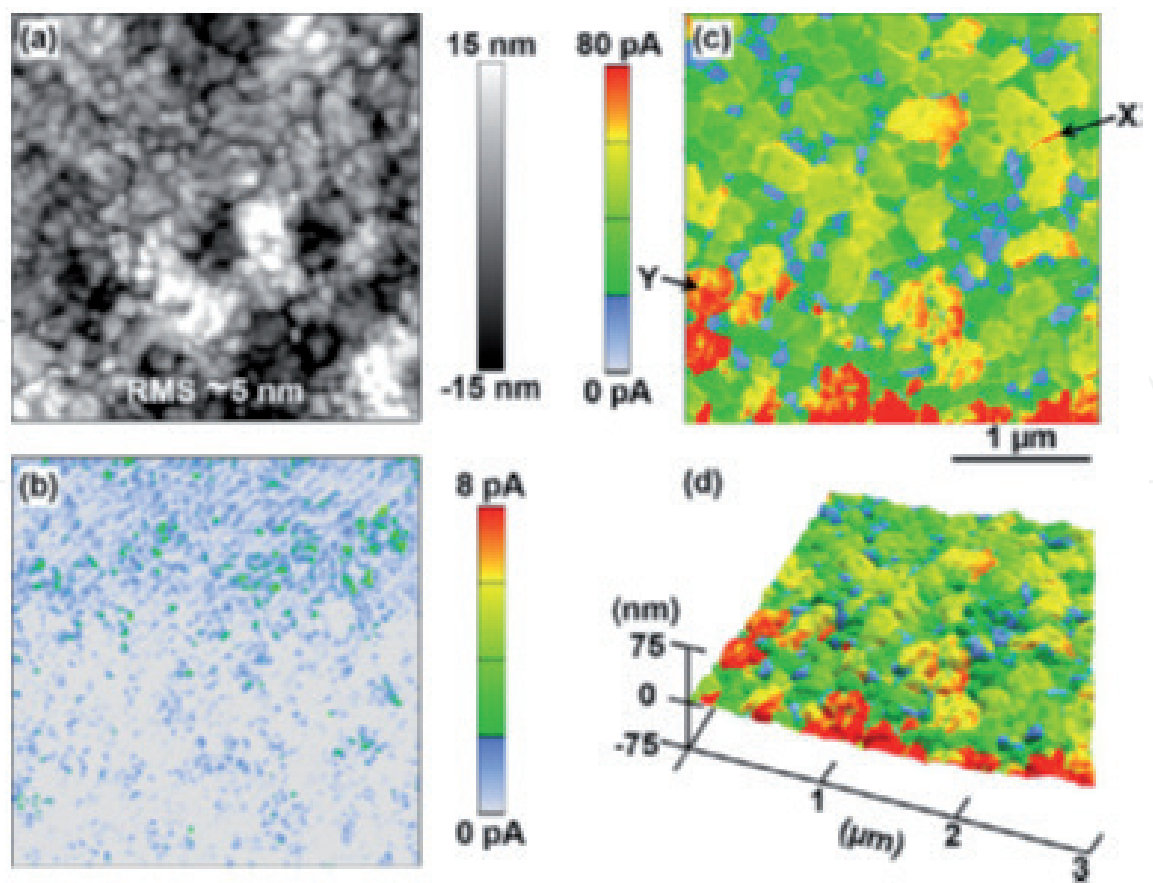


Figure 6. Two-dimensional images of $3\ \mu\text{m} \times 3\ \mu\text{m}$ region of a MAPbI_3 thin film (same magnification): (a) topography, (b) dark I_{sc} , and (c) I_{sc} under $0.07\ \text{W.cm}^{-2}$ illumination. (d) Three-dimensional representation of the topography, overlaid by the illuminated I_{sc} color contrast collected over the same area, revealing the microstructure-specific response. Same current scale for (c,d). Reproduced with permission from [34].

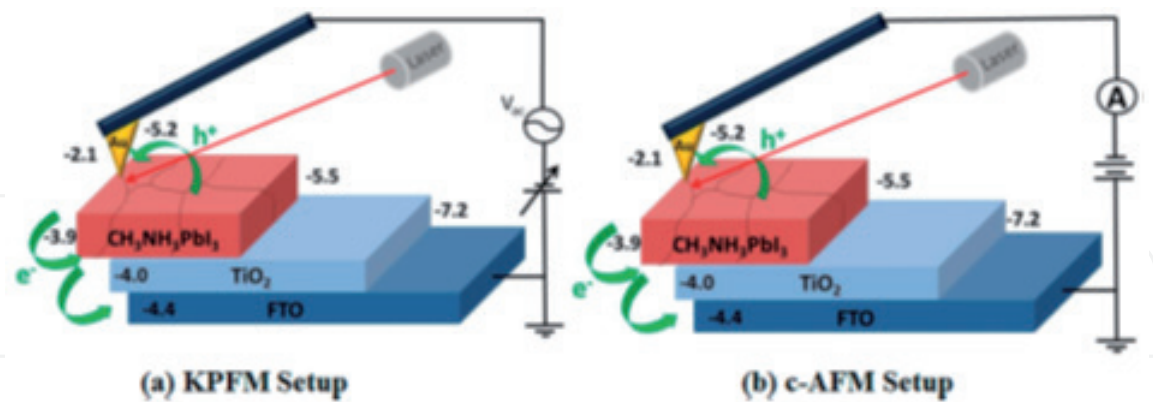


Figure 7. Schematics of the (a) KPFM and (b) C-AFM set up. Relevant vacuum energy levels (in eV) for corresponding materials are indicated. Reproduced with permission from [30].

lower CPD value at GBs and mostly homogeneous mapping which are consistent with the results by Yun *et al.* [30]. Here we illuminated the sample from glass side not from the top (perovskite) side.

Figure 13 shows the topography and surface potential images and line profile of the perovskite films under illumination. The change in the CPD value reflects the change in the work function of the perovskite surface. Charge generation occurs significantly in GBs and the higher photocurrent near GBs suggests that GBs acts as channels for current flow than strong recombination centers. As we know that the higher number of defects are present at the grain boundaries which will increase

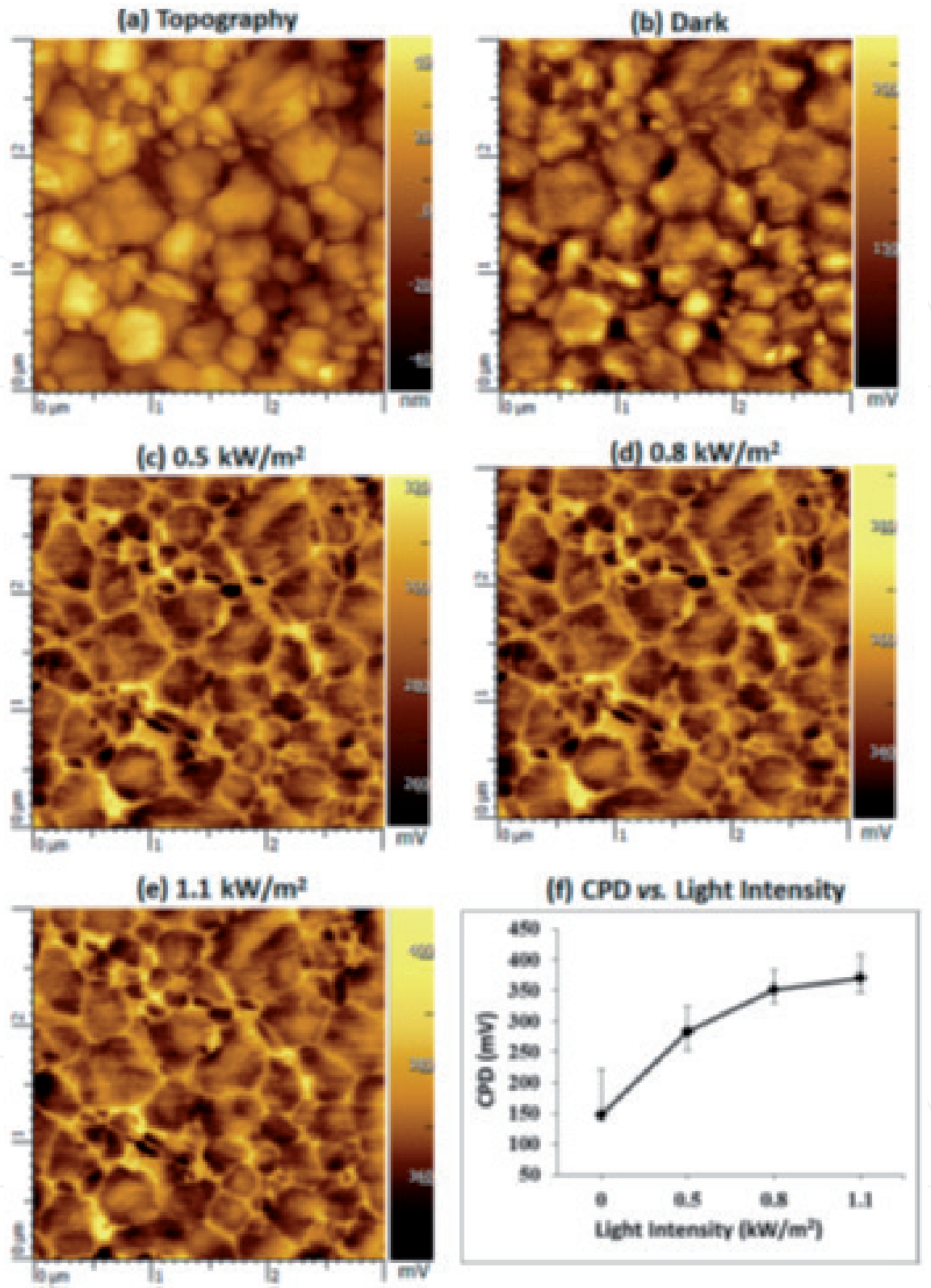


Figure 8. KPFM measurements performed on a $\text{CH}_3\text{NH}_3\text{PbI}_3/\text{TiO}_2/\text{FTO}/\text{glass}$ structure over an area of $3 \mu\text{m}^2$. (a) Topography map and (b) CPD images taken in the dark. (c – e) CPD maps under various laser illumination intensities at a wavelength of 500 nm. (f) Intensity dependence of CPD of the sample at a wavelength of 500 nm as measured by KPFM. Reproduced with permission from [30].

the non-radiative recombination of electrons and holes. The charge accumulation or depletion between grains and GBs may cause band bending, which induces the charge carrier separation. Hence the investigation of electronic properties at grain boundaries is crucial. KPFM has been used to determine the surface potential at

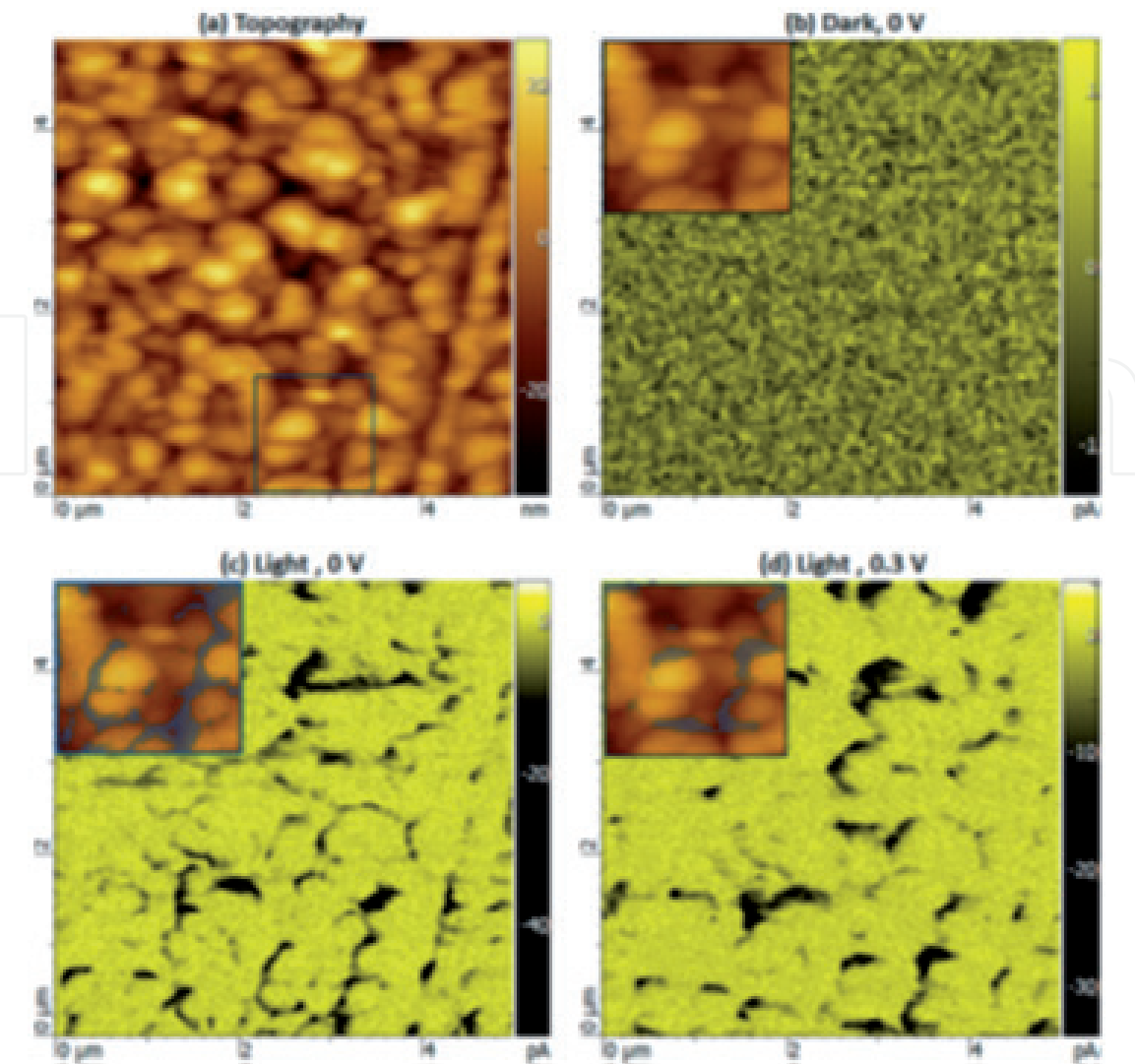


Figure 9. CAFM measurements performed on a $\text{CH}_3\text{NH}_3\text{PbI}_3/\text{TiO}_2/\text{FTO}/\text{glass}$ structure over an area of $5\ \mu\text{m}^2$. (a) Topographic image and (b) current image are taken in the dark at 0 V. current images (c) under illumination at 0 V and (d) under illumination at 0.3 V. insets in panels b – d are overlap of corresponding CAFM maps and a topography map of the region with a white outline in panel a. wavelength and intensity of the illumination were 500 nm and $1.1\ \text{kW}/\text{cm}^2$, . Reproduced with permission from [30].

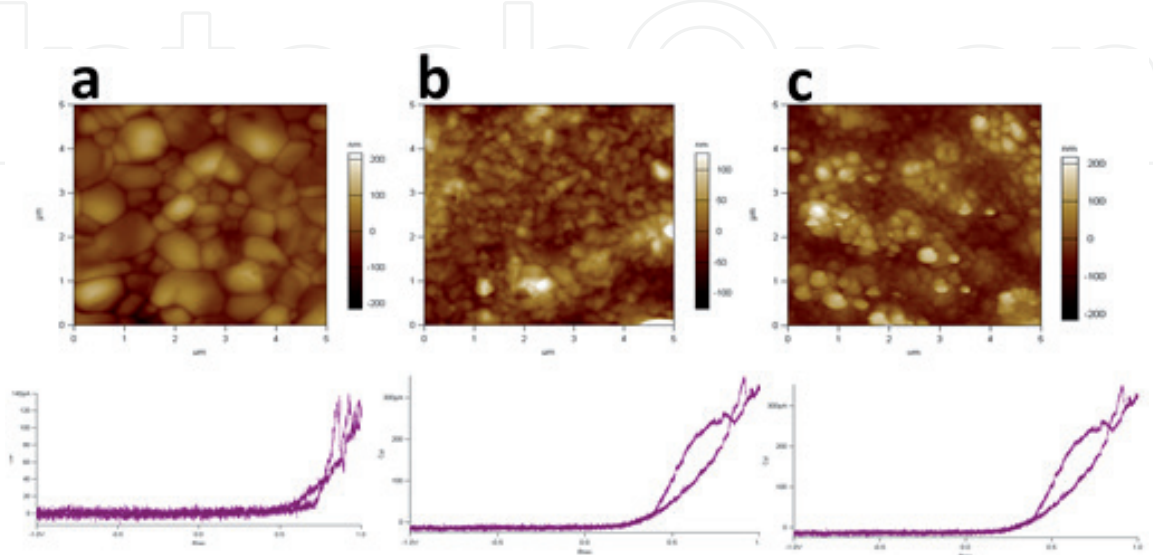


Figure 10. Topography, corresponding current-bias characteristics of MAPI/film annealed at (a) 70° , (b) 90° and (c) $110^\circ\ \text{C}$.

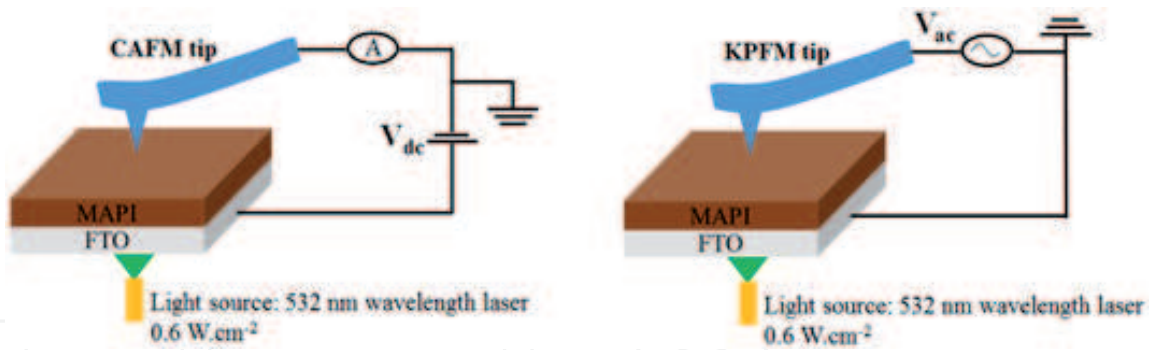


Figure 11.
Schematic representation of CAFM and KPFM measurements.

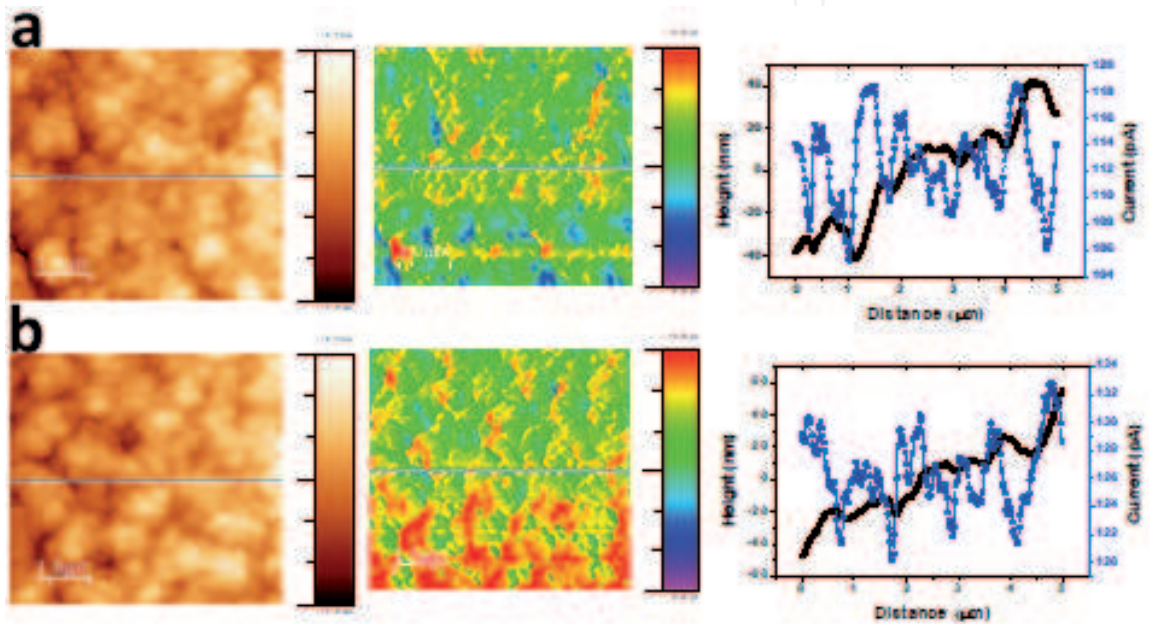


Figure 12.
Topography, current map and line profile of MAPI/FTO (a) dark and (b) under illumination of 532 nm laser having intensity of 0.6 W/cm^2 .

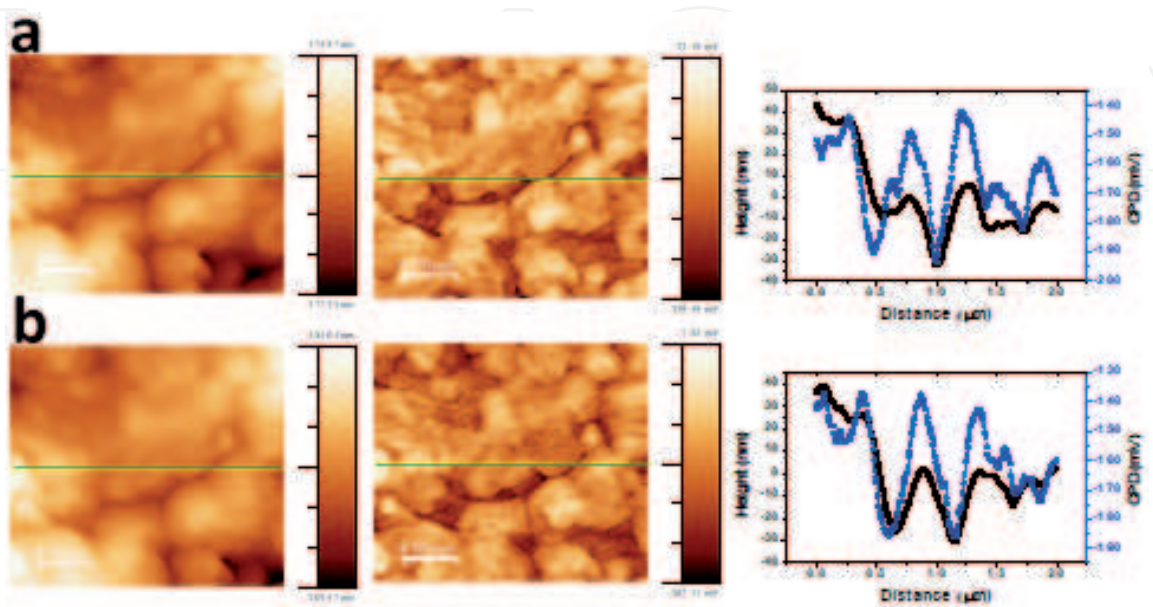


Figure 13.
Topography, CPD map and line profile of MAPI/FTO (a) dark and (b) under illumination of 532 nm laser having intensity of 0.6 W/cm^2 .

grains and GBs. From the topography and CPD map we can see the individual grains and the CPD is higher in grains compared to GBs. The line profile plots are useful in quantitative analysis of CPD variations across topographical feature in perovskite films. CPD is higher at higher region (grains) and lower in lower regions (GBs) and it might be due to the presence of built in potential around the GBs.

4. Conclusion

AFM provides lots of required and interesting results with advanced modes and widely accepted technique to characterize all type of materials. CAFM and KPFM provides information about grains and GBs of photovoltaic materials which help us to understand the current transport and band bending to improve the performance and life time of photovoltaic materials. Combination of such characterization at nanoscale with macroscopic analysis can link the photovoltaic materials properties and optimization of device performance.

Acknowledgements

The author thanks to Prof. Iris Visoly-Fisher, Ben- Gurion University of the Negev, Israel for guidance and support.

Author details

Chandra Shakher Pathak^{1,2}

¹ Ben-Gurion National Solar Energy Center, Department of Solar Energy and Environmental Physics, Jacob Blaustein Institutes for Desert Research, Ben-Gurion University of the Negev, Israel

² Department of Chemical Engineering, Ben-Gurion University of the Negev, Beer Sheva, Israel

*Address all correspondence to: cspathak12@gmail.com

IntechOpen

© 2021 The Author(s). Licensee IntechOpen. This chapter is distributed under the terms of the Creative Commons Attribution License (<http://creativecommons.org/licenses/by/3.0>), which permits unrestricted use, distribution, and reproduction in any medium, provided the original work is properly cited. 

References

- [1] Binning G, Rohrer H, Gerber C, Weibel E. Surface Studies by Scanning Tunneling Microscopy. *Phys Rev Lett* 1982;49:57-61.
- [2] G. Binning, C.F. Quate CG. Atomic Force Microscope. *Phys Rev Lett* 1986;56:930-3. <https://doi.org/10.1201/9781420075250>.
- [3] Nonnenmacher M, O'Boyle MP, Wickramasinghe HK. Kelvin probe force microscopy. *Appl Phys Lett* 1991;58:2921-3. <https://doi.org/10.1063/1.105227>.
- [4] Shirakawa H, Macdiarmid AG. Electrical conductivity in doped polyacetylene. *Phys Rev Lett* 1977;39:1098-101.
- [5] Shirakawa H, Louis EJ, MacDiarmid AG, Chiang CK, Heeger AJ. Synthesis of electrically conducting organic polymers: Halogen derivatives of polyacetylene, (CH)_x. *J Chem Soc Chem Commun* 1977:578-80. <https://doi.org/10.1039/C39770000578>.
- [6] Groenendaal L, Jonas F, Freitag D, Pielartzik H, Reynolds JR. Poly(3,4-ethylenedioxythiophene) and Its Derivatives: Past, Present, and Future. *Adv Mater* 2000;12:481-94. [https://doi.org/10.1002/\(SICI\)1521-4095\(200004\)12:7<481::AID-ADMA481>3.0.CO;2-C](https://doi.org/10.1002/(SICI)1521-4095(200004)12:7<481::AID-ADMA481>3.0.CO;2-C).
- [7] Xia Y, Zhang H, Ouyang J, Yang R, Yang W, Huang F, et al. Highly conductive PEDOT:PSS films prepared through a treatment with zwitterions and their application in polymer photovoltaic cells. *J Mater Chem* 2010;20:9740-7. <https://doi.org/10.1039/c0jm01593h>.
- [8] Pathak CS, Singh JP, Singh R. Effect of dimethyl sulfoxide on the electrical properties of PEDOT:PSS/n-Si heterojunction diodes. *Curr Appl Phys* 2015;15:528-34. <https://doi.org/10.1016/j.cap.2015.01.020>.
- [9] Palumbiny CM, Heller C, Schaffer CJ, Körstgens V, Santoro G, Roth S V, et al. Molecular Reorientation and Structural Changes in Cosolvent-Treated Highly Conductive PEDOT:PSS Electrodes for Flexible Indium Tin Oxide-Free Organic Electronics. *J Phys Chem C* 2014;118:13598-606. <https://doi.org/10.1021/jp501540y>.
- [10] Xia Y, Ouyang J. PEDOT:PSS films with significantly enhanced conductivities induced by preferential solvation with cosolvents and their application in polymer photovoltaic cells. *J Mater Chem* 2011;21:4927. <https://doi.org/10.1039/c0jm04177g>.
- [11] Levermore PA, Jin R, Wang X, Chen L, Bradley DDC, de Mello JC, et al. High efficiency organic light-emitting diodes with PEDOT-based conducting polymer anodes. *J Mater Chem* 2008;18:4414-20. <https://doi.org/10.1039/b805994b>.
- [12] Sun K, Zhang S, Li P, Xia Y, Zhang X, Du D, et al. Review on application of PEDOTs and PEDOT:PSS in energy conversion and storage devices. *J Mater Sci Mater Electron* 2015;26:4438-62. <https://doi.org/10.1007/s10854-015-2895-5>.
- [13] Fan X, Nie W, Tsai H, Wang N, Huang H, Cheng Y, et al. PEDOT:PSS for Flexible and Stretchable Electronics: Modifications, Strategies, and Applications. *Adv Sci* 2019;6:1900813. <https://doi.org/10.1002/advs.201900813>.
- [14] Pathak CS, Kapoor R, Singh JP, Singh R. Investigation of the effect of organic solvents on the electrical characteristics of PEDOT:PSS/p-Si heterojunction diodes. *Thin Solid Films* 2017;622:115-21. <https://doi.org/10.1016/j.tsf.2016.12.030>.

- [15] Pathak CS, Singh JP, Singh R. Modification of electrical properties of PEDOT:PSS/ p -Si heterojunction diodes by doping with dimethyl sulfoxide. *Chem Phys Lett* 2016;652:162-6. <https://doi.org/10.1016/j.cplett.2016.04.029>.
- [16] Pathak CS, Singh JP, Singh R. Optimizing the electrical properties of PEDOT:PSS films by co-solvents and their application in polymer photovoltaic cells. *Appl Phys Lett* 2017;111:102107-5. <https://doi.org/10.1063/1.4994317>.
- [17] Nardes AM, Kemerink M, de Kok MM, Vinken E, Maturova K, Janssen RAJ. Conductivity, work function, and environmental stability of PEDOT:PSS thin films treated with sorbitol. *Org Electron* 2008;9:727-34. <https://doi.org/10.1016/j.orgel.2008.05.006>.
- [18] Berger R, Domanski AL, Weber SAL. file:///J:/AFM/PEDOTPSS for Flexible and Stretchable Electronics Modifications, Strategies, and Applications.pdf. *Eur Polym J* 2013;49:1907-15. <https://doi.org/10.1016/j.eurpolymj.2013.03.005>.
- [19] Pathak CS, Singh JP, Singh R. Preparation of novel graphene-PEDOT : PSS nanocomposite films and fabrication of heterojunction diodes with n -Si. *Chem Phys Lett* 2018;694:75-81. <https://doi.org/10.1016/j.cplett.2018.01.049>.
- [20] Yang S, Yang C, Zhang X, Zheng Z, Bi S, Zhang Y, et al. A conjugated microporous polymer film fabricated by: In situ electro-chemical deposition as a hole transporting layer in organic photovoltaics. *J Mater Chem C* 2018;6:9044-8. <https://doi.org/10.1039/c8tc02933d>.
- [21] Kalachyova Y, Guselnikova O, Postnikov P, Fitl P, Lapcak L, Svorcik V, et al. Reversible switching of PEDOT:PSS conductivity in the dielectric-conductive range through the redistribution of light-governing polymers. *RSC Adv* 2018;8:11198-206. <https://doi.org/10.1039/c7ra12624g>.
- [22] Hosseini E, Ozhukil Kollath V, Karan K. The key mechanism of conductivity in PEDOT:PSS thin films exposed by anomalous conduction behaviour upon solvent-doping and sulfuric acid post-treatment. *J Mater Chem C* 2020;8:3982-90. <https://doi.org/10.1039/c9tc06311k>.
- [23] Kim JY, Jung JH, Lee DE, Joo J. Enhancement of electrical conductivity of poly(3,4-ethylenedioxythiophene)/ poly(4-styrenesulfonate) by a change of solvents. *Synth Met* 2002;126:311-6. [https://doi.org/10.1016/S0379-6779\(01\)00576-8](https://doi.org/10.1016/S0379-6779(01)00576-8).
- [24] Dimitriev OP, Grinko DA, Noskov Y V., Ogurtsov NA, Pud AA. PEDOT:PSS films-Effect of organic solvent additives and annealing on the film conductivity. *Synth Met* 2009;159:2237-9. <https://doi.org/10.1016/j.synthmet.2009.08.022>.
- [25] Pathak CS, Singh JP, Singh R. Effect of dimethyl sulfoxide on the electrical properties of PEDOT:PSS/n-Si heterojunction diodes. *Curr Appl Phys* 2015;15:528-34. <https://doi.org/10.1016/j.cap.2015.01.020>.
- [26] Pathak CS. Investigation of PEDOT:PSS/Si heterojunctions and graphene/Si schottky diodes for potential application in photovoltaics. Published by Indian Institute of Technology Delhi, 2018.
- [27] Melitz W, Shen J, Kummel AC, Lee S. Kelvin probe force microscopy and its application. *Surf Sci Rep* 2011;66:1-27. <https://doi.org/10.1016/j.surfrep.2010.10.001>.
- [28] Pathak CS, Singh JP, Singh R. Organic-inorganic heterojunctions for optoelectronic applications. Published by The Institution of Engineering and

- Technology, 2020. <https://doi.org/10.1049/pbcs049e>.
- [29] best-research-cell-efficiencies. 20200925.pdf n.d.
- [30] Yun JS, Ho-baillie A, Huang S, Woo SH, Heo Y, Seidel J, et al. Benefit of Grain Boundaries in Organic – Inorganic Halide Planar Perovskite Solar Cells. *J Phys Chem Lett* 2015;6:875-80. <https://doi.org/10.1021/acs.jpcclett.5b00182>.
- [31] Li JJ, Ma JY, Ge QQ, Hu JS, Wang D, Wan LJ. Microscopic Investigation of Grain Boundaries in Organolead Halide Perovskite Solar Cells. *ACS Appl Mater Interfaces* 2015;7:28518-23. <https://doi.org/10.1021/acsami.5b09801>.
- [32] Zhao Z, Chen X, Wu H, Wu X, Cao G. Probing the Photovoltage and Photocurrent in Perovskite Solar Cells with Nanoscale Resolution. *Adv Funct Mater* 2016;26:3048-58. <https://doi.org/10.1002/adfm.201504451>.
- [33] Leblebici SY, Leppert L, Li Y, Reyes-Lillo SE, Wickenburg S, Wong E, et al. Facet-dependent photovoltaic efficiency variations in single grains of hybrid halide perovskite. *Nat Energy* 2016;1:1-7. <https://doi.org/10.1038/nenergy.2016.93>.
- [34] Kutes Y, Zhou Y, Bosse JL, Steffes J, Padture NP, Huey BD. Mapping the Photoresponse of CH₃NH₃PbI₃ Hybrid Perovskite Thin Films at the Nanoscale. *Nano Lett* 2016;16:3434-41. <https://doi.org/10.1021/acs.nanolett.5b04157>.
- [35] Xu J, Buin A, Ip AH, Li W, Voznyy O, Comin R, et al. Perovskite-fullerene hybrid materials suppress hysteresis in planar diodes. *Nat Commun* 2015;6:1-8. <https://doi.org/10.1038/ncomms8081>.
- [36] Gomez A, Sanchez S, Campoy-quiles M, Abate A. Topological distribution of reversible and non-reversible degradation in perovskite solar cells. *Nano Energy* 2018;45:94-100. <https://doi.org/10.1016/j.nanoen.2017.12.040>.
- [37] Yang J, Liu X, Zhang Y, Zheng X, He X, Wang H, et al. Comprehensive understanding of heat-induced degradation of triple-cation mixed halide perovskite for a robust solar cell. *Nano Energy* 2018;54:218-26. <https://doi.org/10.1016/j.nanoen.2018.10.011>.
- [38] Formamidinium- P, Lee DS, Yun JS, Kim J, Mahboubi A, Chen S, et al. Passivation of Grain Boundaries by Phenethylammonium in Formamidinium-Methylammonium Lead Halide Perovskite Solar Cells. *ACS Appl Mater Interfaces* 2018;3:647-54. <https://doi.org/10.1021/acsenergylett.8b00121>.
- [39] Faraji N, Qin C, Matsushima T, Adachi C, Seidel J. Grain Boundary Engineering of Halide Perovskite CH₃NH₃PbI₃ Solar Cells with Photochemically Active Additives. *J Phys Chem C* 2018;122:4817-21. <https://doi.org/10.1021/acs.jpcc.8b00804>.
- [40] Yang C, Du P, Dai Z, Li H, Yang X, Chen Q. Effects of Illumination Direction on the Surface Potential of CH₃NH₃PbI₃ Perovskite Films Probed by Kelvin Probe Force Microscopy. *ACS Appl Mater Interfaces* 2019;11:14044-50. <https://doi.org/10.1021/acsami.8b21774>.
- [41] Chen Q, Zhou H, Song T, Luo S, Hong Z, Duan H, et al. Controllable Self-Induced Passivation of Hybrid Lead Iodide Perovskites toward High Performance Solar Cells. *Nano Lett* 2014;14:4158-63. <https://doi.org/10.1021/nl501838y>.
- [42] Liu T, Hu Q, Wu J, Chen K, Zhao L, Liu F, et al. Mesoporous PbI₂ Scaffold for High-Performance Planar Heterojunction Perovskite Solar Cells. *Adv Energy Mater* 2016;6:1-7. <https://doi.org/10.1002/aenm.201501890>.